

DATA-OPTIMIZED CORONAL FIELD MODEL: I. PROOF OF CONCEPT

K. DALMASSE¹, A. SAVCHEVA^{2,3}, S. E. GIBSON⁴, Y. FAN⁴, D. W. NYCHKA⁵, N. FLYER⁴, N. MATHEWS⁶, E. E. DELUCA²

¹ IRAP, Université de Toulouse, CNRS, CNES, UPS, 31028 Toulouse, France

² Harvard-Smithsonian Center for Astrophysics, 60 Garden Street, Cambridge, MA 02138, USA

³ Institute of Astronomy and National Astronomical Observatory, Bulgarian Academy of Sciences, 72 Tsarigradsko Chaussee Blvd., 1784 Sofia, Bulgaria

⁴ National Center for Atmospheric Research, P.O. Box 3000, Boulder, CO 80307-3000, USA

⁵ Department of Applied Mathematics and Statistics, Colorado School of Mines, 1500 Illinois St., Golden, CO 80401, USA and

⁶ Department of Applied Mathematics, University of Colorado at Boulder, 526 UCB, Boulder, CO 80309-0526, USA

Draft version August 9, 2021

ABSTRACT

Deriving the strength and direction of the three-dimensional (3D) magnetic field in the solar atmosphere is fundamental for understanding its dynamics. Volume information on the magnetic field mostly relies on coupling 3D reconstruction methods with photospheric and/or chromospheric surface vector magnetic fields. Infrared coronal polarimetry could provide additional information to better constrain magnetic field reconstructions. However, combining such data with reconstruction methods is challenging, *e.g.*, because of the optical-thinness of the solar corona and the lack and limitations of stereoscopic polarimetry. To address these issues, we introduce the Data-Optimized Coronal Field Model (DOCFM) framework, a model-data fitting approach that combines a parametrized 3D generative model, *e.g.*, a magnetic field extrapolation or a magnetohydrodynamic model, with forward modeling of coronal data. We test it with a parametrized flux rope insertion method and infrared coronal polarimetry where synthetic observations are created from a known “ground truth” physical state. We show that this framework allows us to accurately retrieve the ground truth 3D magnetic field of a set of force-free field solutions from the flux rope insertion method. In observational studies, the DOCFM will provide a means to force the solutions derived with different reconstruction methods to satisfy additional, common, coronal constraints. The DOCFM framework therefore opens new perspectives for the exploitation of coronal polarimetry in magnetic field reconstructions and for developing new techniques to more reliably infer the 3D magnetic fields that trigger solar flares and coronal mass ejections.

Subject headings: polarization – Sun: corona – Sun: magnetic fields

1. INTRODUCTION

Solar flares and coronal mass ejections (CMEs) are driven by the evolution of current-carrying magnetic fields in the solar corona (*e.g.*, Forbes 2000; Priest 2003; Schrijver et al. 2005; Shibata & Magara 2011; Aulanier et al. 2012). Deriving the three-dimensional (3D) properties of such non-potential magnetic fields is critical for identifying the mechanism(s) driving flares and CMEs, as well as for understanding and predicting their evolution (*e.g.*, Bateman 1978; Hood & Priest 1981; Antiochos et al. 1999; Kusano et al. 2012; Pariat et al. 2017). Hence, measuring the strength and direction of the 3D magnetic field in the solar coronal volume is fundamental.

Magnetic field information in the solar corona is mostly derived from the inversion of off-limb polarization measurements associated with the Zeeman and Hanle effects (*e.g.*, Harvey 1969; Casini & Judge 1999; Lin et al. 2004; Centeno et al. 2010). The Zeeman effect creates a frequency-modulated polarization signal sensitive to both the strength and direction of the magnetic field. Due to the large Doppler widths of coronal emission lines and the wavelength squared scaling, the Zeeman effect in the corona is better observed with infrared (IR) spectral lines (*e.g.*, Judge 1998; Penn 2014). However, the coronal magnetic field is weak, with typical values of 1 to 10 Gauss, except right above solar active regions where it can reach up to a few 100 Gauss (*e.g.*, Kuhn et al. 1996; Lin et al. 2000). The corresponding fraction of circular polarization in IR lines, such as the Fe XIII lines, is thus only expected to be of the order of 10^{-4} (equivalent to a 1

Gauss magnetic field strength; *e.g.*, Querfeld 1982; Plowman 2014). Accurately measuring the Zeeman-induced polarization signal in the corona is therefore a challenging task that will require large aperture telescopes, such as the Large Coronagraph (1.5 meter) on the COronal Solar Magnetism Observatory (COSMO; Tomczyk et al. 2016) or the 4-meter Daniel K. Inouye Solar Telescope (DKIST; see Keil et al. 2011, and references therein).

The Hanle effect is the second main mechanism exploited for diagnosing the solar coronal magnetic field. This process modifies the polarization of spectral lines in the presence of a magnetic field (*e.g.*, Hanle 1924; Sahal-Brechot et al. 1977; Bommier & Sahal-Brechot 1982; Arnaud & Newkirk 1987). As opposed to the Zeeman effect, the Hanle effect is a depolarization mechanism. It therefore requires the prior existence of polarization by means of other physical processes such as, *e.g.*, radiation scattering (*e.g.*, Charvin 1965). Sensitivity of the Hanle effect to the magnetic field can range from a few milli-Gauss to several hundred Gauss depending on the choice of spectral line and the strength and direction of the magnetic field (*e.g.*, Bommier & Sahal-Brechot 1982; Raouafi et al. 2016). The Hanle effect is hence a powerful tool for probing the coronal magnetic field, as confirmed by theoretical (*e.g.*, Judge et al. 2006; Rachmeler et al. 2013, 2014; Dalmasse et al. 2016) and observational (*e.g.*, Bąk-Stęślińska et al. 2013; Morton et al. 2016; Gibson et al. 2017; Karna et al. submitted) studies with, *e.g.*, off-limb coronal polarimetry in the IR Fe XIII lines. Note, though, that routine measurements of coronal polarization are currently limited to the IR Fe XIII lines with the Coronal Multi-channel Polarime-

ter (CoMP; Tomczyk et al. 2008) for which the Hanle effect operates in the saturated regime (*e.g.*, Casini & Judge 1999). In practice, it means that the measured linear polarization is sensitive to the magnetic field direction but not its strength. Coronal polarimetry with other spectral lines, such as the IR He I 10830 Å or the UV H I Ly α lines, will be necessary to further obtain Hanle diagnostics sensitive to the coronal magnetic field strength (*e.g.*, Raouafi et al. 2016).

While the Zeeman and Hanle effects offer powerful diagnostics of the coronal magnetic field, determining the actual 3D coronal magnetic field from coronal polarimetry remains a true challenge. In addition to the previously discussed limitations, the solar corona is optically thin at most wavelengths. It follows that the measured polarization signal is the integration of all the plasma emission along the line of sight (LOS). Consequently, it is in general not possible to invert the polarization maps into 2D maps of the magnetic field. Furthermore, it is difficult to extract individual magnetic field data at specific positions along the LOS, even with stereoscopic measurements whether used on their own or combined with 3D magnetic field extrapolation methods (*e.g.*, Kramar et al. 2013, 2016). In particular, one of the main challenges with stereoscopic polarimetry relies on the limited amount of information that can be retrieved from the data, either due to a limited range in magnetic strength sensitivity at a given wavelength, or the lack of it for, *e.g.*, the linear polarization signal measured for the Fe XIII lines. The latter is only sensitive to the magnetic field direction and further possesses both a 90° and 180° ambiguity (saturated regime of the Hanle effect; Judge 2007; Plowman 2014).

Volume information on the vector magnetic field in the solar corona thus mostly relies on the approximate 3D solution obtained by coupling surface magnetic field maps (so-called vector magnetograms), derived from photospheric and/or chromospheric polarimetry, with 3D magnetic field reconstruction methods. 3D techniques for reconstructing the solar coronal magnetic field from surface measurements are either of the nonlinear force-free field (NLFFF; *e.g.*, van Ballegoijen 2004; Wheatland 2007; Wiegmann & Inhester 2010; Valori et al. 2010; Contopoulos et al. 2011; Malanushenko et al. 2012; Amari et al. 2013; Yeates 2014) or the magneto-hydrodynamics (MHD; *e.g.*, Mikić et al. 1999; Inoue et al. 2011; Feng et al. 2012; Zhu et al. 2013) type.

These reconstruction methods differ by the equations solved, the implemented algorithms, and their treatment of the vector magnetograms as boundary conditions (*e.g.*, full vs. LOS vector, pre-processing to create more force-free boundary conditions). As a consequence, the 3D, current-carrying, magnetic field solution and its properties can strongly vary from one method to the other. For instance, De Rosa et al. (2009), DeRosa et al. (2015) and Yeates et al. (2018) reported variations between reconstruction methods that can reach up to 200% for the ratio of free to potential magnetic energy, as well as for relative magnetic helicity, which are key ingredients for producing solar flares and CMEs (*e.g.*, Low 1996; Forbes et al. 2006; Tziotziou et al. 2012; Zuccarello et al. 2018). Even the magnetic topology, which can also play a key role on the stability of the 3D magnetic field configuration (*e.g.*, Gorbachev & Somov 1989; Somov & Verneta 1993; Savcheva et al. 2016), can be strongly affected by the choice of reconstruction method. This can make it difficult to determine the role of magnetic topology in the triggering of solar flares, in particular for events for which some recon-

struction methods may produce a flux rope prior to the flare (*e.g.*, Amari et al. 2018) when others only produce sheared arcades (*e.g.*, Jiang et al. 2016).

The present paper is the first in a series that investigates the possibility of improving the reliability of 3D magnetic field reconstructions by further exploiting coronal polarimetry. The methodology we propose and the tools we use are described in Section 2. Section 3 presents the test-case for which we test and prove the concept of our approach, using a known “ground truth” 3D magnetic field to create synthetic observations. The results of our analysis are reported in Section 4. Section 5 discusses the applicability, limitations and perspectives of our approach. Our conclusions are summarized in Section 6.

2. METHOD

2.1. Summary of approach

The general framework we propose to couple existing 3D magnetic field reconstructions with coronal polarimetric observations is the Data-Optimized Coronal Field Model (DOCFM). It is a model-data fitting approach of the 3D reconstruction of the coronal magnetic field. The DOCFM is built on the three following general bases:

1. A generative 3D magnetic field model (*i.e.*, extrapolation/reconstruction) parametrized through its electric currents. This can be done either at the photospheric boundary (*e.g.*, by means of the transverse magnetic field or the force-free parameter) or in the volume (*e.g.*, for flux rope insertion methods; *e.g.*, van Ballegoijen 2004; Titov et al. 2014, 2018). The generative model then creates the physical state of the corona (*e.g.*, magnetic field, plasma pressure, density, temperature).
2. Forward modeling of coronal polarimetry, in particular to address the fact that the solar corona is optically thin and the lack and limitations of stereoscopic coronal polarimetry.
3. Finding the set of parameters that minimize a cost function (or maximize a likelihood function as in Dalmasse et al. 2016), here the mean squared error between the polarization signal predicted for the magnetic field model and the real polarization data.

Figure 1 presents a general chart of the DOCFM approach.

Previous work has demonstrated the sensitivity of polarization signals in coronal cavities to the 3D magnetic field geometry (*e.g.*, Judge et al. 2006; Bąk-Stęślicka et al. 2013; Rachmeler et al. 2013, 2014). Our main focus is thus on exploiting coronal cavities and their IR polarimetric signatures as observed by CoMP to constrain the 3D magnetic field that precedes CMEs. The parametrized 3D magnetic field model we choose to work with is the flux rope insertion method of van Ballegoijen (2004) briefly presented in Section 2.2. This method uses the LOS measurement of the photospheric magnetic field and an analytical model to produce a coronal flux rope. It is particularly useful for studying coronal cavities, which are likely associated with 3D magnetic flux ropes in weak field regions where the LOS magnetic field is still well-enough above the noise level while the transverse field is not. The flux rope insertion method is thus better suited for studying such structures than more traditional extrapolation techniques for which flux ropes arise from the electric currents associated with the photospheric transverse magnetic

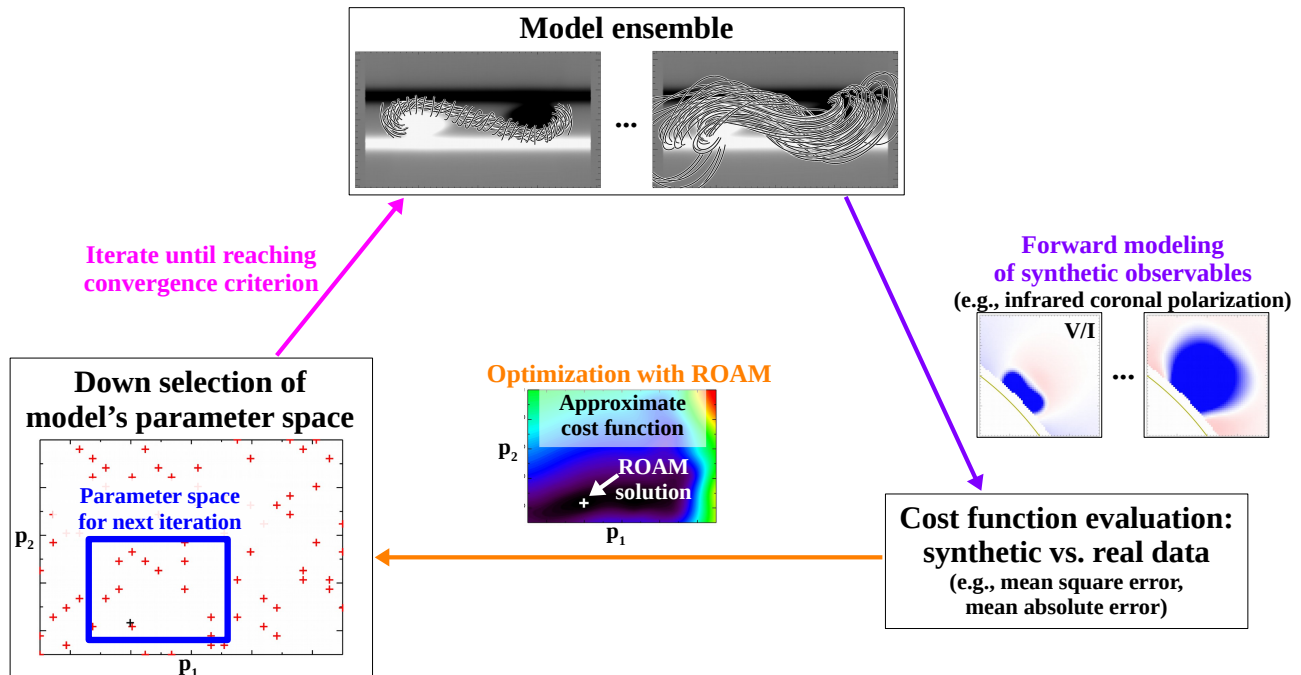


FIG. 1.— General sketch of the DOCFM framework.

field measurements, and which would likely fail to retrieve the flux ropes when such measurements are too noisy. Our choice of synthetic coronal polarimetric data is IR polarimetry in the 10747 Å Fe XIII-I line, synthesized with the codes of the FORWARD¹ IDL package (see Section 2.3; Gibson et al. 2016). For the minimization, we use an iterative implementation of the Radial-basis-functions Optimization Approximation Method (Dalmasse et al. 2016) described in Section 2.4.

2.2. Generative magnetic field model

In the the strong field regions of the solar corona, the plasma β , *i.e.*, the ratio of plasma pressure to magnetic pressure, is relatively low (about 10^{-4} to 10^{-2} ; *e.g.*, Gary 2001). In this low- β environment, all non-magnetic forces (*e.g.*, kinematic plasma flow pressure, gravity) are dominated by the magnetic ones and can thus be neglected. As a consequence, the Lorentz force vanishes (*i.e.*, the magnetic pressure force is compensated by the magnetic tension force) and the coronal magnetic field can be modeled as a force-free field, such that

$$\nabla \times \mathbf{B}(r) = \frac{4\pi}{c} \mathbf{j}(r) = \alpha(r) \mathbf{B}(r), \quad (1)$$

where c is the speed of light, $\mathbf{B}(r)$ is the vector magnetic field, $\mathbf{j}(r)$ is the electric current density and $\alpha(r)$ is the force-free parameter. $\alpha(r) = 0$ refers to the potential field solution, while constant- α solutions are the so-called linear force-free fields (*e.g.*, Alissandrakis 1981). In the most general case, $\alpha(r)$ is constant along individual magnetic field lines, but varies from one field line to the other, which corresponds to the NLFFF solutions (see, *e.g.*, review by Wiegelmann & Sakurai 2012).

Several NLFFF methods have been developed to solve for Equation (1) and extrapolate, or reconstruct, the 3D coronal magnetic field from 2D photospheric magnetic field measurements as a bottom boundary condition (see, *e.g.*, Grad & Rubin 1958; Amari et al. 2006; Wheatland 2007; Valori et al.

2010; Inoue et al. 2012; Malanushenko et al. 2012; Wiegelmann et al. 2012; Titov et al. 2018, to cite a few). In this paper, we use the flux rope insertion method of van Ballegoijen (2004). Such a choice is motivated by the fact that (1) our main focus is on applying the DOCFM approach to coronal cavities, which are density-depleted regions likely associated with a 3D magnetic flux rope (*e.g.*, Bąk-Stęślicka et al. 2013; Gibson 2015), and (2) the flux rope insertion method is already a parametrized 3D generative model. The flux rope possesses two parameters, which are the axial flux (*i.e.*, the magnetic flux along the flux rope axis), Φ , and the poloidal flux per unit length (*i.e.*, the magnetic flux per unit length in the direction perpendicular to the flux rope axis), F .

To apply the flux rope insertion method (van Ballegoijen 2004), a potential field source surface (PFSS) extrapolation is first computed from LOS photospheric magnetograms. EUV data of, *e.g.*, solar filaments (see, *e.g.*, Su et al. 2011; Savcheva et al. 2012), are then used to determine the photospheric feet and path of the flux rope. A field-free (*i.e.*, zero-magnetic field), 3D thin channel is created along the flux rope path in the potential field. The parametrized 3D flux rope is then inserted into that field-free thin channel, thus producing a magnetic field configuration containing a flux rope, but which is out of equilibrium. The magnetic field is then driven towards a quasi-force-free state by means of magnetofrictional relaxation (more details on the flux rope insertion method can be found in, *e.g.*, van Ballegoijen 2004; Bobra et al. 2008; Savcheva et al. 2016). The entire flux rope insertion procedure is performed in terms of modifying and evolving the vector potential, \mathbf{A} (defined by $\mathbf{B} = \nabla \times \mathbf{A}$), through the induction equation and using hyperdiffusion to smooth gradients in the force-free parameter (Yang et al. 1986; van Ballegoijen et al. 2000). The advantage of performing the relaxation with the vector potential is that it automatically ensures that the solenoidal condition for the magnetic field (*i.e.*, $\nabla \cdot \mathbf{B} = 0$) is numerically satisfied.

For all flux rope insertions produced in this paper, the mag-

¹ <http://www.hao.ucar.edu/FORWARD/>

netofrictional relaxation is applied without any diffusion for the first 100 steps. Then, hyperdiffusion is used until 6×10^4 relaxation steps have been performed, at which point the relaxation is stopped and stable NLFFF models are obtained.

2.3. Forward modeling of coronal polarimetry

As mentioned Section 1, the solar corona is optically thin and stereoscopic observations of the coronal polarization are currently not available. In addition, the linear polarization measured in the Fe XIII lines is sensitive to the direction of the coronal magnetic field but not its strength. Hence, off-limb coronal polarimetry as measured by CoMP provides a LOS-integrated signal that cannot be inverted into a 2D plane-of-sky (POS) magnetic field that could be directly plugged in the 3D magnetic field model. To couple such coronal polarimetric data with coronal magnetic field reconstruction models, we must instead rely on a model-data fitting approach. The latter requires a means to produce synthetic coronal observations from a given magnetic field model cube and observing position.

To produce synthetic coronal polarimetric data, we use the FORWARD IDL suite (Gibson et al. 2016). FORWARD is a package for multiwavelength coronal magnetometry that is integrated into the SolarSoft² (Freeland & Handy 1998) IDL toolset. It is designed to create synthetic observables and compare them to coronal data (a full description is provided in Gibson et al. 2016). In particular, FORWARD employs the Coronal Line Emission (CLE) polarimetry code developed by Casini & Judge (1999) to synthesize full Stokes (I, Q, U, V) line profiles for visible and IR forbidden lines including, but not limited to, the Fe XIII lines routinely observed by the CoMP and used in the analyses performed in this paper. Stokes I corresponds to the integrated total line intensity. Stokes (Q, U) are the two components of the linear polarization. And Stokes V is the circular polarization.

2.4. Optimization of flux-ropo parameters

To find the set of parameters minimizing the mean squared error (MSE) between the predicted polarization signal for the magnetic field model and the real data, we use an iterative implementation of the Radial-basis-functions Optimization Approximation Method (ROAM; *e.g.*, Dalmasse et al. 2016). ROAM relies on evaluating a cost function³ (hence, the generative magnetic field model and synthetic observables) for a sparse sample of model-parameter values, approximating the sparse cost function sample with a series of radial basis functions (RBF) to obtain an analytical form for the cost function as a function of the model-parameter values, and computing an estimate of the best-fit parameters by minimizing the analytical form of the cost function (the more detailed procedure is provided in Section 2 of Dalmasse et al. 2016).

The generative magnetic field model we use to test the applicability and accuracy of the DOCFM approach only has two parameters (*cf.* Section 2.2). ROAM was developed to be a fast and efficient optimization method for higher-dimensional optimization problems, *i.e.*, with a number of parameters at least equal to 3. Thus, in practice, there exists other optimization methods that would be faster and more efficient (*i.e.*, requiring fewer model evaluations) than ROAM for

the optimization problem at hand. However, the goal of this paper is to show the applicability of the complete DOCFM framework, which we developed to be general enough to be used with generative magnetic field models having a large number of parameters and for which ROAM is better suited. The latter is the motivation behind the use of ROAM in this investigation.

Let p be the number of (model)-parameters, $\mathbf{x} = (x_1, x_2, \dots, x_p)$ a vector parameter in the p -dimensional parameter space, and $S = \{\mathbf{x}^{i=1, \dots, n}\}$ a random sample of n independent vector parameters (*i.e.*, $x_k^{j \neq i} \neq x_k^i$ for all k). As shown by the tests performed in Dalmasse et al. (2016), the estimate of best-fit parameters obtained with the ROAM can be sensitive to the choice of sample of vector parameters, *i.e.*, to the choice of S . On the other hand, the mean best-fit vector parameter obtained by averaging the best-fit vector parameters computed by applying ROAM with different samples, actually provides a good approximation of the true best-fit vector parameter. We use the latter result to build an iterative implementation of ROAM that gives an estimate of the best-fit vector parameters that is quasi-independent of the sample choice. Our iterative application of ROAM is based on adaptive refinement, such that refinement is performed in the region where the best-fit vector parameter is likely to be. The algorithm is as follows:

1. Let R refer to both the refinement level and iteration number, such that $R = 0$ corresponds to the un-refined starting grid.
2. Choose boundaries, $((x_1^{\min}, x_1^{\max}), \dots, (x_p^{\min}, x_p^{\max})) = ((x_1^{\min, R=0}, x_1^{\max, R=0}), \dots, (x_p^{\min, R=0}, x_p^{\max, R=0}))$, to define the parameter space region where to search for the parameter values minimizing the MSE.
3. Use *latin hypercube sampling* (LHS; *e.g.*, McKay et al. 1979; Iman et al. 1981) to create 3, randomly chosen, sparse samples, (S_1^R, S_2^R, S_3^R) of n vector parameters for the parameter space region of interest. The 3 samples are chosen with the constraint that the $3n$ vector parameters are all different.
4. Combine the latin hypercube samples to produce the 7 samples, $(S'_1, S'_2, S'_3, S'_4, S'_5, S'_6, S'_7) = (S_1^R, S_2^R, S_3^R, S_1^R + S_2^R, S_1^R + S_3^R, S_2^R + S_3^R, S_1^R + S_2^R + S_3^R)$.
5. Apply ROAM to the 7 samples, $(S'_{d=1, \dots, 7})$, to obtain 7 estimates of best-fit vector parameters, $(\mathbf{x}^{\text{bf}, R}(S'_1), \dots, \mathbf{x}^{\text{bf}, R}(S'_7))$, at the R -th iteration.
6. Compute the optimization solution vector defined as the mean best-fit solution, $\mu^R = (\mu_1^R, \mu_2^R, \dots, \mu_p^R)$, and its standard deviation vector, $\sigma^R = (\sigma_1^R, \sigma_2^R, \dots, \sigma_p^R)$, at the R -th iteration

$$\mu_k^R = \frac{1}{7} \sum_{d=1}^7 x_k^{\text{bf}, R}(S'_d) \quad (2)$$

$$\sigma_k^R = \sqrt{\frac{1}{7} \sum_{d=1}^7 (x_k^{\text{bf}, R}(S'_d) - \mu_k^R)^2}, \quad (3)$$

7. Compute the parameter-space boundaries where refine-

² <http://www.lmsal.com/solarsoft/>

³ In essence, minimizing a cost function can be seen as maximizing a (log)-likelihood. ROAM can therefore be used equivalently for maximizing a log-likelihood as in Dalmasse et al. (2016) or minimizing a cost function as in this paper.

TABLE 1
GROUND-TRUTH PARAMETER VALUES

Flux rope model	Φ_{GT} (Mx)	F_{GT} (Mx cm ⁻¹)
Low-height Low-twist (LL)	2.50×10^{20}	-1.00×10^8
Low-height Mild-twist (LM)	2.50×10^{20}	-4.00×10^9
Low-height High-twist (LH)	2.50×10^{20}	-1.00×10^{10}
Mid-height Low-twist (ML)	5.00×10^{20}	-1.00×10^8
Mid-height Mild-twist (MM)	5.00×10^{20}	-4.00×10^9
Mid-height High-twist (MH)	5.00×10^{20}	-1.00×10^{10}
High-height Low-twist (HL)	7.50×10^{20}	-1.00×10^8
High-height Mild-twist (HM)	7.50×10^{20}	-4.00×10^9
High-height High-twist (HH)	7.50×10^{20}	-1.00×10^{10}

NOTE. — Each model is used to produce a set of coronal polarimetric observations to be fitted, as if we were applying the DOCFM to 9 different cavity systems in observational applications. Such a choice allows us to show that the robustness and success of the DOCFM framework are independent of the choice of parameter values for the ground truth 3D magnetic field.

ment is needed according to

$$x_k^{\min,R+1} = \frac{(\lambda - 1) x_k^{\min,R} + \min(x_k^{\text{bf}}(S'_1), \dots, x_k^{\text{bf}}(S'_7))}{\lambda} \quad (4)$$

$$x_k^{\max,R+1} = \frac{(\lambda - 1) x_k^{\max,R} + \max(x_k^{\text{bf}}(S'_1), \dots, x_k^{\text{bf}}(S'_7))}{\lambda}, \quad (5)$$

where $\lambda > 1$ is the shrinkage coefficient. It is a user-specified scalar that controls the speed at which the refining region shrinks; larger λ values lead to slower shrinkage.

- Repeat steps 3 through 7 for the refined region until a convergence criterion is met (*e.g.*, σ_k^R and/or the refining region are sufficiently small).

3. TEST-CASE

3.1. Ground-truth magnetic fields

With this series of papers, our goal is to investigate the possibility of improving the reliability of 3D magnetic field reconstructions by further exploiting coronal polarimetry. The primary goal of this investigation is to prove the concept of the methodology and characterize the uncertainties that are both inherent to the limited amount of information contained in the polarimetric data (see Section 1) and the limitations of the optimization algorithm (described in Section 2.4). To that end, we begin by creating a “ground truth” solution, which is a full representation of the coronal physical state (magnetic field, density, temperature, pressure) created from a generative model. With this ground truth solution, we can forward model synthetic coronal data that will be used in the place of true observations. The point of such an approach is to test the capability of the DOCFM framework for a problem where the solution is fully known.

Limitations due to the ability of the generative model to reproduce a given magnetic field will be addressed in our second paper in this series (Paper II). For these reasons, the ground-truth magnetic fields we use in this paper are created with the reconstruction model we use, *i.e.*, the flux rope insertion method briefly described in Section 2.2.

To produce a ground-truth magnetic field with the flux rope insertion method, we first need a photospheric magnetic flux distribution and a flux rope path (see Section 2.2). Figure 2

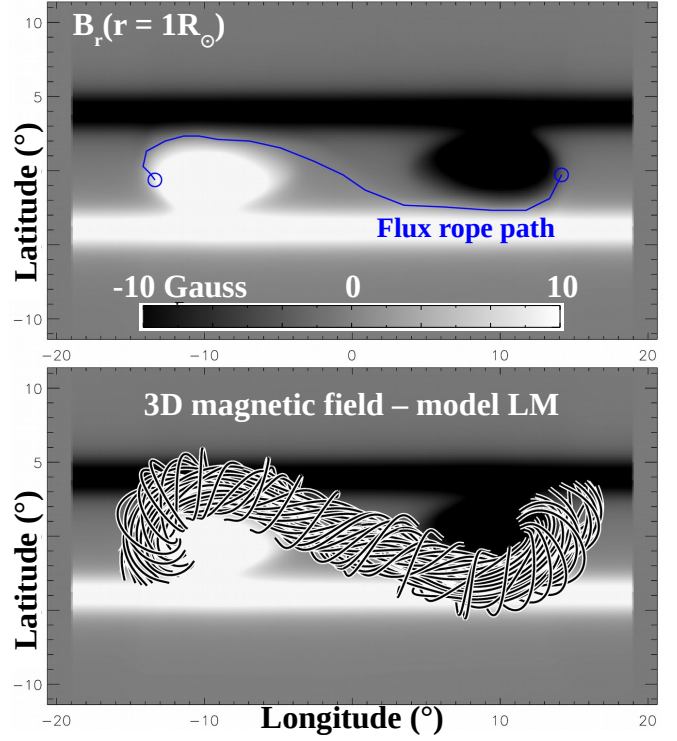


FIG. 2.— **Top:** Photospheric magnetic flux distribution (grey scale) and flux rope path (blue line) and feet (blue circles) used to prove the concept of the DOCFM approach with the flux rope insertion method, as given from Fan (2012) MHD simulation. The magnetic field is in units of Gauss. **Bottom:** Top view of selected 3D magnetic field lines for ground-truth model LM which parameter values are reported in Table 1.

displays the photospheric magnetogram and flux rope path selected for our investigation. The boundary condition is chosen to be consistent with that of flux-rope MHD model of Fan (2012), which we will use in Paper II to further test the robustness of our approach. For consistency, we computed the PFSS from the flux distribution displayed in Figure 2 with the source surface set at $\approx 6R_\odot$, which is far enough from the photosphere to allow most of the arcade magnetic field to be closed. To create the ground-truth, current-carrying magnetic field, we then insert a flux rope with axial flux, Φ_{GT} , and poloidal flux per unit length, F_{GT} . Figure 2 displays the ground-truth solution defined by the set of parameters, $\Phi_{GT} = 2.5 \times 10^{20}$ Mx and $F_{GT} = -4 \times 10^9$ Mx \cdot cm⁻¹, which produces a low-lying, mildly-twisted, left-handed flux rope referred to as model LM.

To show that the DOCFM approach works regardless of the choice of ground-truth parameters, (Φ_{GT}, F_{GT}) , and validate it, we consider 8 additional ground truth solutions that are reported in Table 1. Each one of the 9 chosen flux ropes is used to create a set of coronal polarimetric observations to be fitted, as if we were applying the DOCFM framework to finding the 3D magnetic field of 9 different solar coronal cavities. In particular, we produce low-height, mid-height and high-height ground truth flux ropes with different degrees of magnetic twist by choosing different axial and poloidal flux values.

3.2. Synthetic data

Our application of the DOCFM framework has a focus on the exploitation of off-limb coronal polarimetry as obtained by the CoMP instrument in the Fe XIII-I line (10747 Å;

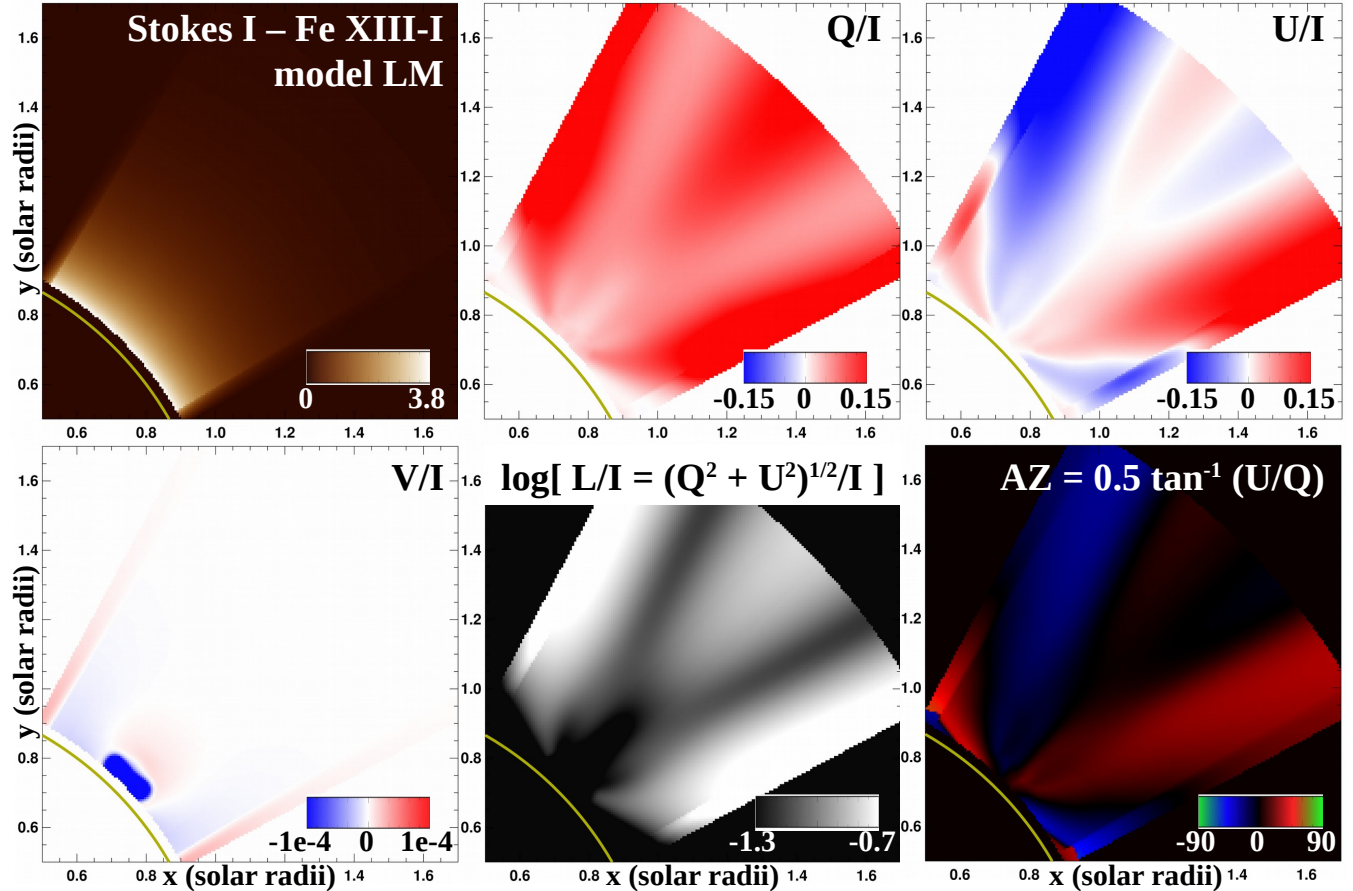


FIG. 3.— Coronal polarimetric observations in the Fe XIII-I line synthesized with FORWARD for the ground-truth model LM which parameter values are reported in Table 1. The flux rope axis is aligned with the LOS. The total line intensity (Stokes I), the two components of the fraction of linear polarization (Q/I and U/I), and the fraction of circular polarization (V/I) are displayed together with the fraction of linear ($L/I = \sqrt{Q^2 + U^2}/I$) polarization and the azimuth ($AZ = 0.5 \tan^{-1}(U/Q)$). Notice the darkening in the central part of the flux rope and the dark lagomorph shape in the L/I signal, which are typical signatures expected in the L/I signal associated with flux ropes closely aligned with the LOS (e.g., Bąk-Stęślicka et al. 2013; Rachmeler et al. 2013).

Tomczyk et al. 2008). For our analysis, we use Stokes I , Q , U and V images synthesized with FORWARD (see Section 2.3). We further considered Stokes $L = \sqrt{Q^2 + U^2}$ and Stokes $AZ = 0.5 \tan^{-1}(U/Q)$ images, which provide an alternate representation of the linear polarization and have been shown to provide useful diagnostics of the coronal magnetic field (e.g., Bąk-Stęślicka et al. 2013; Rachmeler et al. 2014; Gibson et al. 2017; Karna et al. submitted). Each synthetic Stokes image is generated with a field of view (FOV) set to $y \times z = [0.5R_\odot, 1.7R_\odot]^2$ (y and z being the plane-of-sky coordinates) and $x = [-0.79, 0.79]R_\odot$ in the LOS direction. The POS and the LOS are respectively covered with 192^2 and 161 grid points. The resulting spatial resolution is $\approx 6.0'' \times 6.0''$ in the POS, and $\approx 9.4''$ along the LOS. The forward calculations of the Stokes parameters are limited to a radial range of $[1.03, 1.7]R_\odot$, where 1.03 corresponds to the lower limit of CoMP FOV. Our choice of spatial resolution of $6.0''$ is only slightly lower than that of CoMP ($4.5''$) to allow us to maintain a relatively low computational time per set of Stokes parameters (about 15 minutes on a Linux workstation with an Intel Xeon E5-2630 v4 processor).

Forward modeling of coronal polarimetric observables requires a 3D magnetic field model and also a plasma model, because the density and temperature are involved in the formation process of any emission line. However, most NLFFF generative models, such as the flux rope insertion one, dis-

regard the plasma and only provide a 3D magnetic field solution. In the DOCFM framework, we therefore need to provide a plasma model if the magnetic field reconstruction model does not include one. For a FFF, the plasma solution compatible with the force-free assumption is a spherically symmetric hydrostatic atmosphere. If we further assume that the atmosphere is isothermal with coronal temperature, T_c , then the plasma density and pressure are

$$n(r) = n_c \exp\left(\frac{R_c}{h} \cdot \frac{R_c - r}{r}\right) \quad (6)$$

$$h = \frac{2k_B T_c R_c^2}{GM_c m_p} \quad (7)$$

$$P(r) = 2n(r)k_B T_c, \quad (8)$$

where r is the radial distance to the center of the Sun (in cm), R_c is the radius of the solar coronal base, $n_c = n(R_c)$ is the plasma density at the coronal base (in units of cm^{-3}), $n(r)$ is the coronal plasma density (in units of cm^{-3}), h is the scale height (in cm), $k_B = 1.38 \times 10^{-16}$ erg K^{-1} is Boltzmann constant (in CGS units), $G = 6.67 \times 10^{-8}$ $\text{cm}^3 \text{g}^{-1} \text{s}^{-2}$ is the gravitational constant (CGS units), M_c is the solar plasma mass at R_c (in g), $m_p = 1.67 \times 10^{-24}$ g is the proton mass, and $P(r)$ is the plasma pressure (in dyne cm^{-2}).

Equations (6)–(8) define the plasma model we specify with each magnetic field model we compute in this paper. Assum-

ing that the coronal base is at ~ 2 Mm above the photosphere, then we have $R_c \approx R_\odot = 6.96 \times 10^{10}$ cm (the solar radius) and $M_c \approx M_\odot = 1.99 \times 10^{33}$ g (the solar mass). We set $T_c = 1.46 \times 10^6$ K and $n_c = 1.82 \times 10^8$ cm $^{-3}$ in accordance with the values observed at the base of the 3D MHD simulation of Fan (2012) for consistency with Paper II (cf. Section 3.1). The resulting coronal polarimetric observations for the ground-truth model LM described Section 3.1 are shown in Figure 3.

3.3. Mean squared error diagnostics

In the DOCFM framework, the 3D magnetic field solution is obtained by minimization of an MSE between predicted and real polarization signals. Let Y be a Stokes-related image, *i.e.*, Y can be any of $\{Q/I, U/I, V/I, L/I, AZ\}$. Working with images of polarization fraction is here motivated by the fact that Stokes I, Q, U and V all have dependencies on the plasma density (*e.g.*, Casini & Judge 1999) and that working with ratios of these quantities reduces the sensitivity to the plasma density. Y^{GT} is a Stokes-related image associated with the ground-truth magnetic field, *i.e.*, any of the images shown in Figure 3. For the i -th vector parameter, \mathbf{x}^i , the mean squared error, $\chi_Y^2(\mathbf{x}^i)$, between the predicted ($Y(\mathbf{x}^i)$) and ground-truth images, is

$$\chi_Y^2(\mathbf{x}^i) = \sum_l (Y_l(\mathbf{x}^i) - Y_l^{\text{GT}})^2, \quad (9)$$

where l is the l -th pixel of the Y image. The final MSEs we consider are then

$$\chi_{QUV}^2(\mathbf{x}^i) = w_{Q/I} \chi_{Q/I}^2(\mathbf{x}^i) + w_{U/I} \chi_{U/I}^2(\mathbf{x}^i) + w_{V/I} \chi_{V/I}^2(\mathbf{x}^i) \quad (10)$$

$$\chi_{QU}^2(\mathbf{x}^i) = w_{Q/I} \chi_{Q/I}^2(\mathbf{x}^i) + w_{U/I} \chi_{U/I}^2(\mathbf{x}^i) \quad (11)$$

$$\chi_{LAZV}^2(\mathbf{x}^i) = w_{L/I} \chi_{L/I}^2(\mathbf{x}^i) + w_{AZ} \chi_{AZ}^2(\mathbf{x}^i) + w_{V/I} \chi_{V/I}^2(\mathbf{x}^i) \quad (12)$$

$$\chi_{LAZ}^2(\mathbf{x}^i) = w_{L/I} \chi_{L/I}^2(\mathbf{x}^i) + w_{AZ} \chi_{AZ}^2(\mathbf{x}^i), \quad (13)$$

where the w_Y coefficients are used to force the individual MSEs to similarly contribute to the overall MSE. Such a choice is motivated by the fact that, $Q/I, U/I, V/I, L/I$, and AZ vary on very different scales, *i.e.*, $\sim 10^{-2}$ for $(Q/I, U/I, L/I)$, $\sim 10^{-4}$ for V/I , and $\sim 1 - 10^2$ for AZ (see *e.g.*, Judge et al. 2006; Rachmeler et al. 2013; Gibson et al. 2017). By tuning the w_Y coefficients, we can make sure that the overall MSE is sensitive to the individual MSE possessing the smallest scale and not dominated by the one with the largest scale. The values used for our analysis are $(w_{Q/I}, w_{U/I}, w_{L/I}, w_{AZ}, w_{V/I}) = (5.4 \times 10^{-2}, 6.1 \times 10^{-2}, 4.5 \times 10^{-2}, 1.7 \times 10^{-3}, 7.5 \times 10^3)$.

CoMP is currently the only instrument realizing daily observations of coronal emission line polarization in the IR Fe XIII lines. Unfortunately, the signal-to-noise ratio for the circular polarization (Stokes V) is too small for CoMP to allow its routine measurement. Although this limitation should be resolved by DKIST or the proposed COSMO telescope (Tomczyk et al. 2016), we use the χ_{QU}^2 MSE to test whether the linear polarization signal associated with the Fe XIII lines contains sufficient information to fully constrain the coronal magnetic field in our model-data fitting approach. Finally, although observations of the linear polarization actually provide Stokes Q and U , insights at the actual 3D coronal magnetic field are better obtained from the visual inspection of Stokes L and AZ . The MSEs with Stokes L and AZ are chosen to investigate which of (L, AZ) or (Q, U) provides the most use-

ful numerical constraints in our application of the DOCFM framework.

3.4. Error analysis

To characterize the uncertainties in our model-data fitting approach of the 3D reconstruction of solar coronal magnetic fields, we compute the following errors

$$\epsilon_\Phi = \left| \frac{\Phi_{\text{BF}} - \Phi_{\text{GT}}}{\Phi_{\text{GT}}} \right| \quad (14)$$

$$\epsilon_F = \left| \frac{F_{\text{BF}} - F_{\text{GT}}}{F_{\text{GT}}} \right| \quad (15)$$

$$\epsilon_B = \sqrt{\frac{1}{N} \sum_m \left(\frac{\|\mathbf{B}_m^{\text{BF}}\| - \|\mathbf{B}_m^{\text{GT}}\|}{\|\mathbf{B}_m^{\text{GT}}\|} \right)^2} \quad (16)$$

$$\epsilon_{B\text{-angle}} = \sqrt{\frac{1}{N} \sum_m \theta_m^2} \quad (17)$$

$$\epsilon_{B\text{-CWL}} = \sin^{-1} \left(\frac{\sum_m \|\mathbf{B}_m^{\text{BF}}\| \sin(\theta_m)}{\sum_m \|\mathbf{B}_m^{\text{BF}}\|} \right) \quad (18)$$

$$\epsilon_J = \sqrt{\frac{1}{N} \sum_i \left(\frac{\|\mathbf{j}_m^{\text{BF}}\| - \|\mathbf{j}_m^{\text{GT}}\|}{\|\mathbf{j}_m^{\text{GT}}\|} \right)^2} \quad (19)$$

$$\epsilon_{J\text{-angle}} = \sqrt{\frac{1}{N} \sum_m \alpha_m^2} \quad (20)$$

$$\epsilon_{J\text{-CWL}} = \sin^{-1} \left(\frac{\sum_m \|\mathbf{j}_m^{\text{BF}}\| \sin(\alpha_m)}{\sum_m \|\mathbf{j}_m^{\text{BF}}\|} \right) \quad (21)$$

$$\epsilon_{E_{\text{free}}} = \left| \frac{E_{\text{free}}(\mathbf{B}_{\text{BF}}) - E_{\text{free}}(\mathbf{B}_{\text{GT}})}{E_{\text{free}}(\mathbf{B}_{\text{GT}})} \right| \quad (22)$$

$$\epsilon_{H_r} = \left| \frac{H_r(\mathbf{B}_{\text{BF}}) - H_r(\mathbf{B}_{\text{GT}})}{H_r(\mathbf{B}_{\text{GT}})} \right| \quad (23)$$

$$\epsilon_Y = \sqrt{\frac{1}{N'} \sum_l (Y_l^{\text{BF}} - Y_l^{\text{GT}})^2}, \quad (24)$$

where the subscript m runs over the grid points of the 3D magnetic field computational domain, N is the number of grid points, E_{free} and H_r respectively are the free magnetic energy and the relative magnetic helicity as computed in Bobra et al. (2008), the subscript l runs over the pixels of the synthetic Stokes image $Y = \{I, Q, U, V\}$, N' is the number of pixels in

TABLE 2
OPTIMIZATION RESULTS VS. ITERATION NUMBER
FOR GROUND-TRUTH MODEL LM WITH χ^2_{QUV} MINIMIZATION

R	Φ_{BF} (Mx)	σ_Φ (Mx)	F_{BF} (Mx cm $^{-1}$)	σ_F (Mx cm $^{-1}$)
0	2.55×10^{20}	2.58×10^{19}	-5.53×10^8	1.73×10^{10}
1	2.51×10^{20}	3.66×10^{18}	-3.93×10^9	2.84×10^9
2	2.51×10^{20}	8.09×10^{17}	-3.65×10^9	5.61×10^8
3	2.50×10^{20}	2.46×10^{17}	-4.00×10^9	2.18×10^8

NOTE. — $\mu = (\Phi_{BF}, F_{BF})$ and $\sigma = (\sigma_\Phi, \sigma_F)$ are the mean and standard deviation values computed from the seven best-fit vector parameters obtained at each iteration of ROAM, as defined by Equations (2) and (3) in Section 2.4. The ground-truth model LM is defined by $(\Phi_{GT}, F_{GT}) = (2.50 \times 10^{20}$ Mx, -4.00×10^9 Mx cm $^{-1}$).

the synthetic Stokes image, and

$$\theta_m = \sin^{-1} \left(\frac{\|\mathbf{B}_m^{BF} \times \mathbf{B}_m^{GT}\|}{\|\mathbf{B}_m^{BF}\| \|\mathbf{B}_m^{GT}\|} \right) \quad (25)$$

$$\alpha_m = \sin^{-1} \left(\frac{\|\mathbf{j}_m^{BF} \times \mathbf{j}_m^{GT}\|}{\|\mathbf{j}_m^{BF}\| \|\mathbf{j}_m^{GT}\|} \right). \quad (26)$$

ϵ_Φ , ϵ_F , ϵ_B , ϵ_J , $\epsilon_{E_{\text{free}}}$ and ϵ_{H_r} are relative errors. ϵ_Y is in units of parts per million (ppm). $\epsilon_{B\text{-angle}}$, $\epsilon_{B\text{-CWL}}$, $\epsilon_{J\text{-angle}}$, and $\epsilon_{J\text{-CWL}}$ are angles in units of degrees. Note that $\epsilon_{B\text{-CWL}}$ and $\epsilon_{J\text{-CWL}}$ are CW-like (CWL) angles defined in the spirit of Equations (13) and (14) of Wheatland et al. (2000).

4. RESULTS

4.1. Optimization results

To apply the DOCFM approach, we fix the un-refined starting parameter space grid to $\Phi(\text{Mx}) \times F(\text{Mx cm}^{-1}) = [10^{20}, 10^{21}] \times [-5 \times 10^{10}, +5 \times 10^{10}]$. Four models with axial fluxes spanning four orders of magnitude (10^{19} , 10^{20} , 10^{21} , 10^{22}) were first run to restrict the axial flux, Φ , to a range of values always strong enough to produce a flux rope above the polarity inversion line, and low enough to ensure that the flux rope insertion (Section 2.2) can lead to a stable flux rope (stable in the sense that the flux rope does not erupt during the magnetofrictional relaxation stage; cf. Section 2.2). For the optimization steps with ROAM, we use 3 LHS of 24 points at each iteration, resulting in the computation of 72 flux rope models per iteration. For each iteration, the 72 flux rope models are generated (including the magnetofrictional relaxation phase; see Section 2.2) in parallel using the high-performance computing (HPC) resources of the CALMIP⁴ supercomputing center, which provides us with the advantage that one iteration has an elapsed time equivalent to the generation of one flux rope model only. For the computation of the new boundaries where refinement is to be done at each iteration (see Equations (4) and (5)), we set the shrinkage coefficient to $\lambda = 2$.

Table 2 reports the optimization results obtained when applying the DOCFM approach to reconstructing the 3D magnetic field of the flux rope model LM from the minimization of the χ^2_{QUV} MSE defined in Equation (10). It shows that convergence towards a best-fit solution is achieved in only 4 applications (*i.e.*, $R = 3$ iterations) of the optimization procedure described in Section 2.4, which corresponds to 288 model evaluations. The best-fit solution, as computed from Equations (2), is obtained for $\Phi_{BF} = 2.50 \times 10^{20}$ Mx $\pm 2.46 \times 10^{17}$ and $F_{BF} = -4.00 \times 10^9$ Mx cm $^{-1} \pm 2.18 \times 10^8$, while the ground-truth parameters for model LM are $(\Phi_{GT}, F_{GT}) = (2.50 \times 10^{20}$ Mx, -4.00×10^9 Mx cm $^{-1}$). Our model-data fitting approach is therefore able to accurately retrieve the ground-truth parameters of the flux rope model LM.

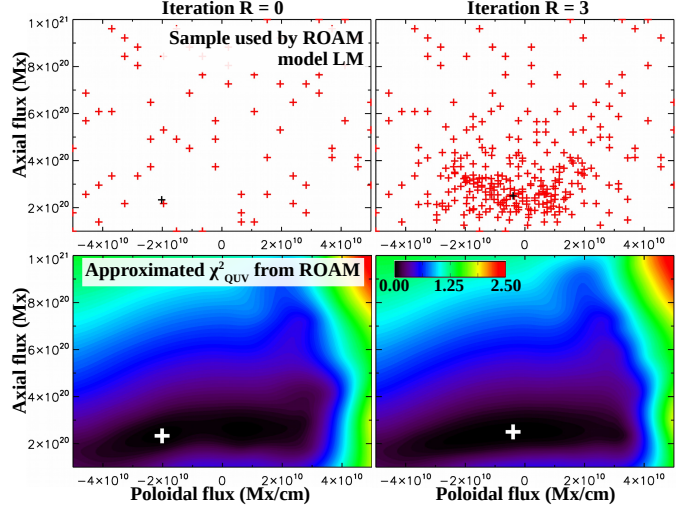


FIG. 4.— Optimization results for sample S'_7 (see Section 2.4) at the un-refined starting stage (left column) and at the refined final stage (right column) for model LM (see Table 1 for its parameter values). **Top:** Distribution of models in the parameter space (red “+” signs). **Bottom:** Corresponding approximated χ^2_{QUV} MSE (defined by Equation (10)). The black (top row) / white (bottom row) “+” sign indicates the position of the minimum found by ROAM.

TABLE 3
OPTIMIZATION RESULTS FOR ALL MEAN SQUARED ERROR TESTS
FOR GROUND-TRUTH MODEL LM

Minimized MSE	Φ_{BF} (Mx)	σ_Φ (Mx)	F_{BF} (Mx cm $^{-1}$)	σ_F (Mx cm $^{-1}$)
χ^2_{QUV}	2.50×10^{20}	2.46×10^{17}	-4.00×10^9	2.18×10^8
χ^2_{QU}	2.50×10^{20}	1.32×10^{17}	-3.93×10^9	8.85×10^7
χ^2_{LAZV}	2.50×10^{20}	2.17×10^{17}	-4.00×10^9	1.85×10^8
χ^2_{LAZ}	2.50×10^{20}	9.12×10^{16}	-3.98×10^9	4.75×10^7

NOTE. — $\mu = (\Phi_{BF}, F_{BF})$ and $\sigma = (\sigma_\Phi, \sigma_F)$ are the mean and standard deviation values computed from the seven best-fit vector parameters obtained after $R = 3$ iterations of ROAM, as defined by Equations (2) and (3) in Section 2.4. The ground-truth model LM is defined by $(\Phi_{GT}, F_{GT}) = (2.50 \times 10^{20}$ Mx, -4.00×10^9 Mx cm $^{-1}$).

tion (2), is obtained for $\Phi_{BF} = 2.50 \times 10^{20}$ Mx $\pm 2.46 \times 10^{17}$ and $F_{BF} = -4.00 \times 10^9$ Mx cm $^{-1} \pm 2.18 \times 10^8$, while the ground-truth parameters for model LM are $(\Phi_{GT}, F_{GT}) = (2.50 \times 10^{20}$ Mx, -4.00×10^9 Mx cm $^{-1}$). Our model-data fitting approach is therefore able to accurately retrieve the ground-truth parameters of the flux rope model LM.

Table 2 further details the mean, $\mu = (\Phi_{BF}, F_{BF})$, and standard deviation, $\sigma = (\sigma_\Phi, \sigma_F)$, values computed from the seven best-fit vector parameters obtained at each iteration of ROAM, as defined by Equations (2) and (3). The standard deviation value reflects the disagreement between these seven best-fit vector parameters. The table shows that the standard deviation tends to display very high values at the first application of the optimization procedure and progressively decreases as the number of iteration increases. For the first few iterations, this is because the seven best-fit vector parameters can strongly depend on the sparse sample used to apply ROAM (*cf.* Dalmasse et al. 2016). As the optimization procedure is iterated, this disagreement decreases and the seven best-fit vector parameters eventually converge towards the same solution, which only marginally depends on the sparse sample used with ROAM. Therefore, the proposed iterative imple-

⁴ <https://www.calmip.univ-toulouse.fr/>

TABLE 4
OPTIMIZATION RESULTS VS. GROUND-TRUTH PARAMETERS FOR χ^2_{QUV} MINIMIZATION

Flux rope model	Φ_{GT} (Mx)	Φ_{BF} (Mx)	σ_Φ (Mx)	F_{GT} (Mx cm ⁻¹)	F_{BF} (Mx cm ⁻¹)	σ_F (Mx cm ⁻¹)	R_f
LL	2.50×10^{20}	2.50×10^{20}	3.46×10^{16}	-1.00×10^8	-1.08×10^8	2.43×10^7	5
LM	2.50×10^{20}	2.50×10^{20}	2.46×10^{17}	-4.00×10^9	-4.00×10^9	2.18×10^8	3
LH	2.50×10^{20}	2.50×10^{20}	2.86×10^{17}	-1.00×10^{10}	-0.98×10^{10}	1.35×10^8	3
ML	5.00×10^{20}	5.00×10^{20}	3.46×10^{16}	-1.00×10^8	-1.02×10^8	6.79×10^6	4
MM	5.00×10^{20}	5.00×10^{20}	3.14×10^{16}	-4.00×10^9	-4.03×10^9	1.21×10^7	3
MH	5.00×10^{20}	5.00×10^{20}	7.48×10^{16}	-1.00×10^{10}	-1.00×10^{10}	1.48×10^7	3
HL	7.50×10^{20}	7.50×10^{20}	3.19×10^{17}	-1.00×10^8	-0.93×10^8	3.05×10^7	3
HM	7.50×10^{20}	7.49×10^{20}	6.36×10^{17}	-4.00×10^9	-3.95×10^9	1.26×10^7	3
HH	7.50×10^{20}	7.50×10^{20}	2.24×10^{17}	-1.00×10^{10}	-1.00×10^{10}	4.02×10^7	3

NOTE. — $\mu = (\Phi_{BF}, F_{BF})$ and $\sigma = (\sigma_\Phi, \sigma_F)$ are the mean and standard deviation values computed from the seven best-fit vector parameters obtained at the final iteration of ROAM, R_f , as defined by Equations (2) and (3) in Section 2.4.

mentation of ROAM (see Section 2.4) makes it more robust against the choice of sparse sample used to apply it.

The results reported in Table 2 also show that the poloidal flux parameter, F_{BF} , is systematically associated with a much higher standard deviation than the axial flux parameter, Φ_{BF} , and requires more iterations for the seven best-fit vector parameters to converge towards a consistent solution. From the analysis of the approximated MSE (shown in Figure 4), we find that this is related with the fact that the minimum region is very flat and extended, and hence poorly defined for the poloidal flux as compared with the axial flux. The latter is explained by the fact that, within the setup considered in this work, the set of polarimetric data exploited to reconstruct the 3D coronal magnetic field is much more sensitive to the axial flux of the flux rope than to its poloidal flux. These polarization data thus provide stronger constraints on the former than on the latter. This, however, only applies to the setup considered in this paper and would require additional investigations to determine whether it is true regardless of, *e.g.*, the flux rope axis orientation with regard to the LOS-direction.

The optimization results for all MSE tests for this ground-truth model LM are presented in Table 3, after $R = 3$ iterations. At intermediate iteration steps (not shown here), we do not systematically find a one-to-one correspondence between the seven best-fit vector parameters obtained from the χ^2_{LAZV} -minimization and those obtained from the χ^2_{QUV} -minimization. This can be explained by the fact that the two datasets bring constraints on the 3D coronal magnetic field in different forms, which results in different MSE surfaces and shapes that ROAM necessarily approximates differently. However, the spread of these seven best-fit vector parameters remains very similar regardless of the iteration number and dataset used. Once convergence is achieved, the differences between the solution, (Φ_{BF}, F_{BF}) , from the χ^2_{LAZV} -minimization and that from the χ^2_{QUV} -minimization are only marginal. For the tests and setup considered in this paper, we thus do not find any clear evidence that performing the optimization with the $\{L/I, AZ, V/I\}$ dataset provides a particular advantage or disadvantage over using the $\{Q/I, U/I, V/I\}$ dataset. Further investigations with different LHS distributions and magnetic field models are required to determine whether this is a general trend.

Table 3 further compares the optimization results obtained when only the linear polarization signal (*i.e.*, $\{L/I, AZ\}$ or $\{Q/I, U/I\}$) is used with the DOCFM approach. It shows

that, once convergence is achieved, the solution obtained from minimizing χ^2_{QU} (resp. χ^2_{LAZ}) is only marginally different from the solution obtained when minimizing χ^2_{QUV} (resp. χ^2_{LAZV}). While it does not mean that it will always be the case in modeling and/or observational studies, we find that the fraction of linear polarization and the azimuth together contain enough information to constrain the 3D coronal magnetic field. This is a combination of the van Vleck effect (Van Vleck 1925) and magnetic flux component along the LOS. Both produce extinctions in the linear polarization signal that carry information about both the POS and LOS magnetic field components (as already described in previous studies; see, *e.g.*, Bąk-Stęślicka et al. 2013; Rachmeler et al. 2014; Gibson et al. 2017; Karna et al. submitted), and hence about the coronal electric current system. Such signatures are enough to constrain the original 3D magnetic field and retrieve its ground-truth parameters with the DOCFM method.

Finally, the results of applying the DOCFM approach to all 9 flux rope ground-truth models reported in Table 1 are presented in Table 4 for χ^2_{QUV} minimization. It shows that our model-data fitting method is able to accurately retrieve the ground-truth parameters of each flux rope model, regardless of their values. The analysis of these 9 tests as a function of iteration number and dataset used for the χ^2 minimization confirms all our previous findings.

4.2. 3D magnetic field comparison

We now focus on the qualitative and quantitative comparison of the 3D magnetic field solution obtained by the DOCFM method and the actual ground-truth magnetic field. Figure 5 displays the 3D magnetic field lines for the flux rope model LM (panel (a)) and the DOCFM solution (panels (b) to (e)), which parameter values are reported in Table 3) obtained from each χ^2 minimization defined by Equations (10) – (13). The flux rope field-lines from the DOCFM solutions were all integrated from the same selected starting footpoints as the ground-truth magnetic field lines. As one can see from the colored arrows, differences exist between the DOCFM solution and the ground-truth magnetic field lines (*i.e.*, compare panels (b – e) to panel (a)). However, these differences are very small and the 3D magnetic field is – qualitatively – very well recovered, regardless of the dataset used to perform the χ^2 minimization. The latter is further confirmed by the one-to-one comparison of the 3D vector magnetic field in the volume as defined per Equations (16) – (18) and reported in Table 5.

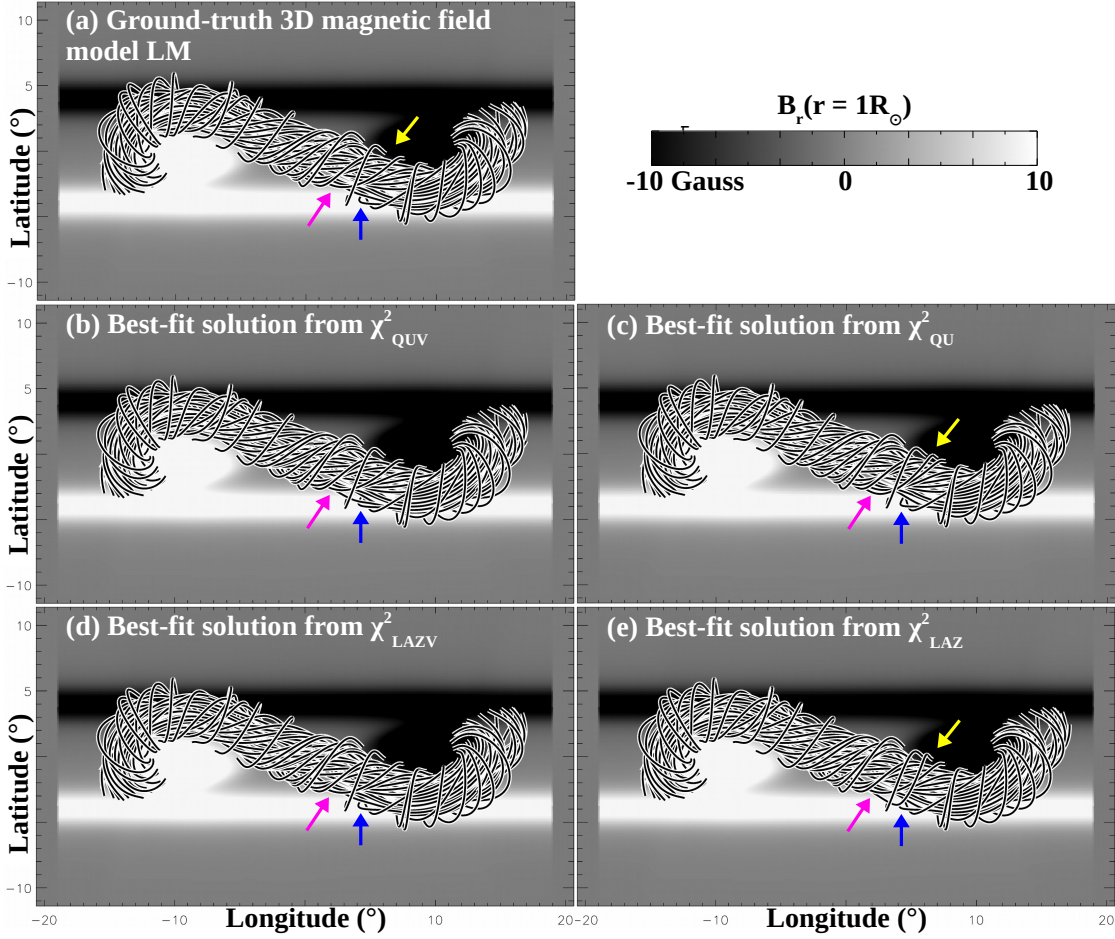


FIG. 5.— Top view of the selected field-lines from (a) the ground-truth magnetic field model LM (see Table 1 for its parameter values) and (b – e) the optimization solutions (reported in Table 3) associated with the χ^2_{QUV} , χ^2_{QU} , χ^2_{LAZV} , and χ^2_{LAZ} MSEs defined in Equations (10) – (13). The field-lines from the DOCFM solutions were all integrated from the same selected starting footpoints as the ground-truth magnetic field lines. A few colored arrows have been added to emphasize regions where magnetic field lines are different from the ground-truth magnetic field ones.

TABLE 5
BEST-FITS VS. GROUND-TRUTH 3D MAGNETIC FIELD
FOR FLUX ROPE MODEL LM

Error	Upper value from the 4 solutions obtained with χ^2_{QUV} , χ^2_{QU} , χ^2_{LAZV} and χ^2_{LAZ}
ϵ_Φ	4.47×10^{-4}
ϵ_F	1.64×10^{-2}
ϵ_B	5.34×10^{-4}
$\epsilon_{B\text{-angle}}$	2.44×10^{-2}
$\epsilon_{B\text{-CWL}}$	4.08×10^{-2}
ϵ_J	3.13×10^{-2}
$\epsilon_{J\text{-angle}}$	1.38
$\epsilon_{J\text{-CWL}}$	1.93×10^{-1}
$\epsilon_{E_{\text{free}}}$	1.38×10^{-3}
ϵ_{H_r}	1.09×10^{-3}
ϵ_l	1.26×10^{-5}
ϵ_Q	2.40×10^{-5}
ϵ_U	1.66×10^{-5}
ϵ_V	1.70×10^{-7}

NOTE. — All ϵ are errors defined by Equations (14) – (24). ϵ_Φ , ϵ_F , ϵ_B , ϵ_J , $\epsilon_{E_{\text{free}}}$ and ϵ_{H_r} are relative errors. ϵ_l , ϵ_Q , ϵ_U and ϵ_V are Stokes errors in ppm. $\epsilon_{B\text{-angle}}$, $\epsilon_{B\text{-CWL}}$, $\epsilon_{J\text{-angle}}$ and $\epsilon_{J\text{-CWL}}$ are angle errors in degrees. For brevity and because values are very similar regardless of the nature of the minimized MSE, only the largest errors found are displayed.

TABLE 6
BEST-FITS VS. GROUND-TRUTH 3D MAGNETIC FIELD
FOR χ^2_{QUV} MINIMIZATION

Error	Upper value from the solutions obtained for all flux rope types of Table 4
ϵ_Φ	1.41×10^{-3}
ϵ_F	7.64×10^{-2}
ϵ_B	1.19×10^{-3}
$\epsilon_{B\text{-angle}}$	5.41×10^{-2}
$\epsilon_{B\text{-CWL}}$	9.01×10^{-2}
ϵ_J	5.52×10^{-2}
$\epsilon_{J\text{-angle}}$	1.34
$\epsilon_{J\text{-CWL}}$	3.41×10^{-1}
$\epsilon_{E_{\text{free}}}$	2.88×10^{-3}
ϵ_{H_r}	1.99×10^{-3}
ϵ_l	3.08×10^{-5}
ϵ_Q	5.98×10^{-5}
ϵ_U	5.24×10^{-5}
ϵ_V	4.18×10^{-7}

NOTE. — All ϵ are errors defined by Equations (14) – (24). ϵ_Φ , ϵ_F , ϵ_B , ϵ_J , $\epsilon_{E_{\text{free}}}$ and ϵ_{H_r} are relative errors. ϵ_l , ϵ_Q , ϵ_U and ϵ_V are Stokes errors in ppm. $\epsilon_{B\text{-angle}}$, $\epsilon_{B\text{-CWL}}$, $\epsilon_{J\text{-angle}}$ and $\epsilon_{J\text{-CWL}}$ are angle errors in degrees. Results are representative of the errors obtained from minimizing all the other MSEs considered in the paper. For brevity and because values are very similar regardless of the flux rope type, only the largest errors found are displayed.

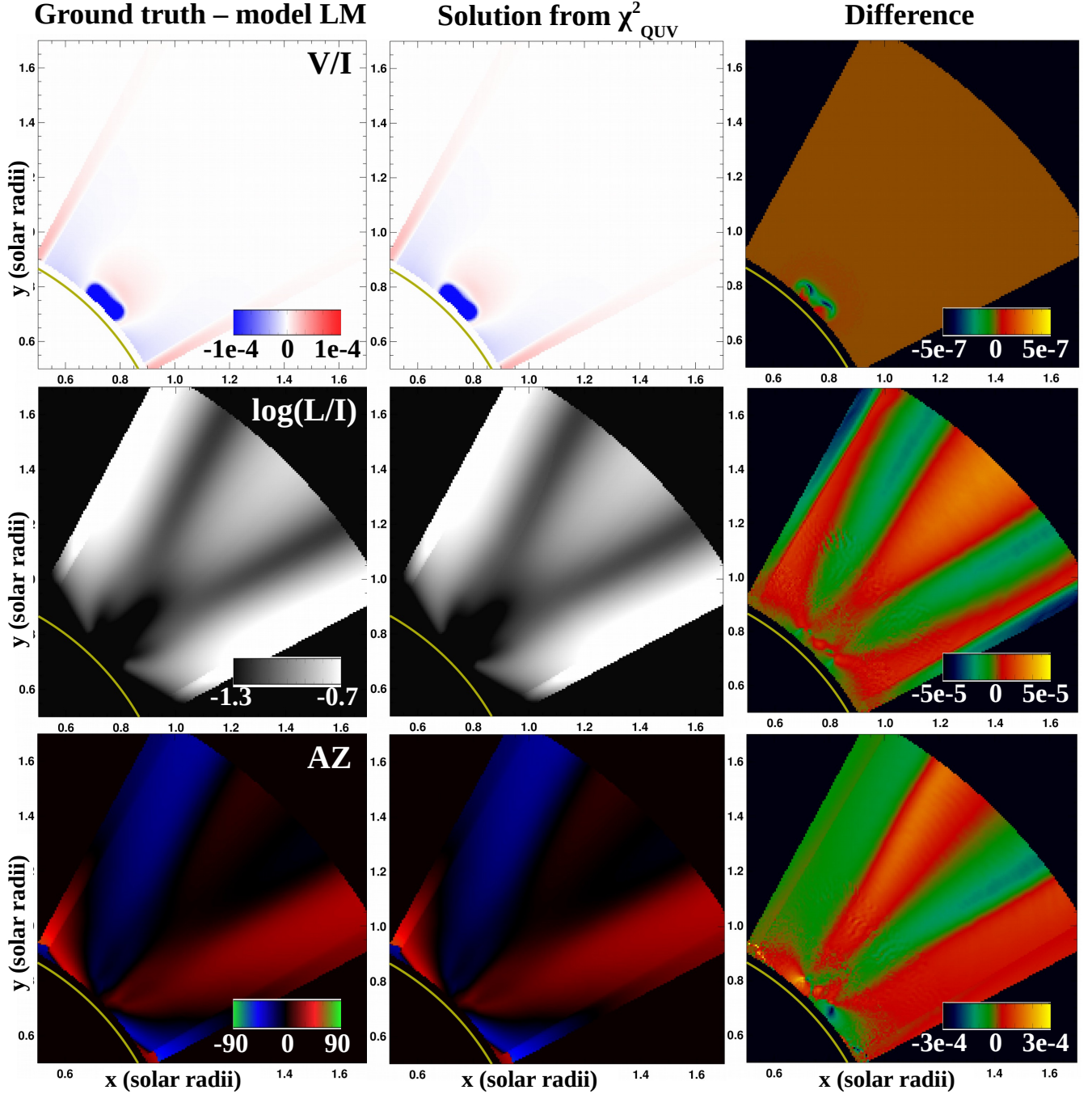


Fig. 6.— Comparison between Stokes-related images for the ground-truth magnetic field model LM (see Table 1 for its parameter values) and for the solution obtained from the χ^2_{QUV} MSE defined in Equation (10).

Indeed, we find that the relative error for the magnetic field strength is below 0.06%, hence very low, while the error on the magnetic field direction is below 0.05° (whether analyzed from Equation (17) or Equation (18)).

The high accuracy on retrieving the ground-truth 3D magnetic field translates into a good accuracy for all magnetic field-related quantities considered in this paper. The errors on the electric current density strength and direction (Equations (19) – (21)) are larger than for the magnetic field, as one would expect since the electric current density is related to the gradients of the magnetic field and spatial derivatives tend to enhance errors. However, the errors remain marginal since

the electric current density strength is recovered with a relative error lower than 4% and its direction with an error lower than 1.4° . Similarly, we find good results for global quantities such as the free magnetic energy and the relative magnetic helicity, which are recovered with a relative error below 0.2%. The same is true for the synthetic polarization data (Table 5) and their related quantities (e.g., L/I , V/I and AZ shown Figure 6), for which the errors are typically 10^3 times smaller than the actual polarization signal.

The very high quality of these results is agnostic to the minimized MSE (Table 5) and flux rope model used to produce the ground-truth synthetic observations (Table 6). We there-

fore conclude that the DOCFM approach allows us to accurately retrieve the 3D coronal magnetic field when the coronal polarization dataset to be fitted originates from a solution of the generative model (here, the flux rope insertion method). The DOCFM framework thus opens new perspectives for coupling photospheric magnetic field data to coronal polarimetry in 3D reconstruction of the solar coronal magnetic field.

5. DISCUSSION

As previously mentioned, DOCFM is a framework we propose to couple existing 3D magnetic field reconstructions with coronal polarimetric observations. It is a model-data fitting approach of the 3D reconstruction of the coronal magnetic field. It combines a parametrized generative magnetic field model, forward modeling techniques, and an optimization method for finding the magnetic field parameters that minimize the differences between the real data and synthetic observables predicted for the magnetic field model.

Although we applied and tested the DOCFM approach using the flux rope insertion method and coronal polarimetry, it should be emphasized that the proposed framework was developed in a way that is agnostic to the generative magnetic field model, the type of coronal data used to constrain the 3D magnetic field (off-limb and on-disk), and the optimization method (although ROAM was specifically designed for the DOCFM to be tractable even with computationally-heavy generative models having 3 parameters or more). The DOCFM is thus general enough to be used with any type of generative magnetic field model, whether it is, *e.g.*, an extrapolation method (including flux rope insertion; Wheatland et al. 2000; van Ballegooijen 2004; Wiegmann 2004; Valori et al. 2005; Amari & Aly 2010; Contopoulos et al. 2011; Titov et al. 2014), an MHD model (*e.g.*, Mikić et al. 1999; Inoue et al. 2011; Feng et al. 2012; Zhu et al. 2013), or even an analytical one. The only constraint is that the generative model must be parametrized either through, *e.g.*, its magnetic field or its electric currents. Similarly, DOCFM can be used with any type of solar data, both off-limb and on-disk, provided that it can be forward modeled. This is the case for, *e.g.*, white-light/EUV/X-ray imaging or radio polarimetry through, *e.g.*, the FORWARD IDL suite (see Gibson et al. 2016, and references therein).

In this paper, we showed that the DOCFM framework is applicable and allows one to accurately retrieve the 3D coronal magnetic field when the coronal synthetic observations are created from a known ground-truth physical state solution of the parametrized generative model. It should be emphasized, though, that DOCFM does not guarantee that the obtained solution will be the true, 3D, coronal magnetic field in both observational and – more general – modeling applications. Indeed, the ability of the DOCFM to provide the true coronal magnetic field entirely depends on the ability of the generative model to reproduce the true coronal magnetic field. That point will be addressed and further discussed in Paper II (in preparation). Thus, the DOCFM method is to be seen as a tool to directly include more observational constraints in extrapolations/reconstructions of the 3D coronal magnetic field, with the goal of obtaining better solutions. At this point, it should be mentioned that applying the DOCFM approach with un-parametrized extrapolation/reconstruction methods can be achieved without modifying the generative model technique, as long as parametrization is achieved through, *e.g.*, the photospheric vector magnetic field. The DOCFM approach therefore opens interesting

new perspectives for investigating whether it may help different extrapolation methods to converge towards much more similar solutions, as well as for developing new reconstruction techniques to more accurately and robustly derive the 3D coronal magnetic field and its properties (*e.g.*, 3D distribution of coronal electric currents, magnetic topology, free magnetic energy, relative magnetic helicity) by combining photospheric and coronal data.

In the investigations presented here, the orientation of the flux rope with regard to the LOS was not considered as a parameter to be fitted, although it might affect the fitting results. Current observational applications of the DOCFM approach with off-limb coronal data and a flux rope insertion method requires the use of on-disk data, *e.g.*, magnetogram and EUV emission, prior to (resp. after) the passage at the West (resp. East) limb to determine both the photospheric feet and insertion path of the flux rope. Then, the cube containing the 3D magnetic field model can either be rigidly rotated to the limb for fitting the off-limb coronal data or evolved by means of a photospheric flux transport model to take into account the evolution due to both differential rotation and granular motions (see *e.g.*, Yeates et al. 2007, and references therein). In both cases, the orientation of the flux rope axis with regard to the LOS should thus be very well constrained. Note also that potential fitting issues due to uncertainties on the flux rope orientation with regard to the LOS would be completely removed in the case of fitting on-disk coronal data and/or using multi-viewpoint simultaneous observations taken 90 degrees apart (*i.e.*, typically when the ESA/Solar Orbiter will be in quadrature with Earth, thus providing photospheric vector magnetograms and EUV flux rope data from atop, while Earth will be providing off-limb coronal observations of the flux rope from the side).

Finally, we recall that the forward modeling of coronal polarimetry (and most other coronal data) requires a 3D plasma density and temperature model (Gibson et al. 2016), which is not provided by NLFFF extrapolation/reconstruction models such as the one used in this paper but could be provided by MHD models. Although using ratios of Stokes images (*e.g.*, Q/I instead of Q) should help reducing the dependency of the Stokes-related images, and hence of the DOCFM solution, to the plasma density model, it may not completely suppress it. For this reason, future investigations with more complex and realistic plasma density and temperature models will be required to fully characterize the sensitivity of the DOCFM 3D magnetic field solution to the plasma model. Such investigations will be particularly useful to determine how complex and realistic the plasma model really needs to be to reliably apply the DOCFM framework in observational studies. On the other hand, plasma solutions derived from tomographic inversions (*e.g.*, Frazin 2000; Frazin et al. 2005; Kramar et al. 2009; Barbey et al. 2013; Guennou et al. 2012; Huang et al. 2012) and/or line intensity ratios may provide a good solution to that problem in observational applications.

6. CONCLUSIONS

Deriving the 3D magnetic field in the volume of the solar atmosphere is critical for improving our understanding of solar activity and evolution (see reviews by *e.g.*, Forbes et al. 2006, and references therein). Most present solar magnetic field data rely on the inversion of 2D photospheric and chromospheric polarization measurements (*e.g.*, Lagg et al. 2017). Such data only provide surface vector magnetic fields at the lowest layers of the solar atmosphere. 3D models, *e.g.*, in

the form of NLFFF and/or MHD solutions (see review by *e.g.*, Wiegmann et al. 2014, and references therein), coupled to photospheric and/or chromospheric surface vector magnetograms are then required to construct an approximate 3D magnetic field solution in the solar corona. Unfortunately, the inferred 3D solution and its properties can strongly depend on the chosen 3D reconstruction method (De Rosa et al. 2009; DeRosa et al. 2015; Yeates et al. 2018). On the other hand, coronal polarization data could provide additional information to better constrain the 3D coronal magnetic field (*e.g.*, Casini & Judge 1999; Rachmeler et al. 2013; Gibson et al. 2017). However, combining them with 3D reconstruction methods is not straightforward. In particular, such measurements cannot – in general – be inverted into 2D maps of vector magnetic fields that could be directly integrated into reconstruction methods (see *e.g.*, line-of-sight integration issue and limitations of stereoscopic measurements in Section 1).

In this paper, we introduced the Data-Optimized Coronal Field Model (DOCFM), a new framework for coupling existing 3D magnetic field reconstruction techniques with coronal polarimetric data. The DOCFM is a model-data fitting approach of the 3D magnetic field reconstruction problem. It relies on the parametrization of 3D reconstruction methods through their electric currents (*e.g.*, surface parametrization at the photosphere or volume parametrization) and the fine-tuning of the electric current-related parameters such that the polarization signal predicted for the magnetic field model (*i.e.*, through forward modeling; Gibson et al. 2016) matches the real polarization data.

By applying it with the flux rope insertion method of van Ballegoijen (2004) and IR coronal polarimetry in the Fe XIII lines as observed by the CoMP, we have demonstrated the applicability of the DOCFM methodology. We showed that coronal polarimetric data contain enough information to constrain the 3D coronal magnetic field solution when coupled with a parametrized 3D flux rope insertion method. While it

does not guarantee that the inferred magnetic field solution is the true coronal magnetic field in observational applications, the DOCFM approach provides a means to force coronal magnetic field reconstructions to satisfy additional, common, coronal constraints. This framework therefore opens new perspectives for the exploitation of coronal polarimetry in 3D reconstructions of the solar coronal magnetic field.

Ideally, the application of the DOCFM methodology requires simultaneous measurements of photospheric and/or chromospheric vector magnetic fields viewed near solar disk center and off-limb coronal polarization. The Earth's vantage point alone does not permit co-spatial and co-temporal observations of this type. The upcoming ESA/Solar Orbiter space mission will enable such opportunities when Solar Orbiter will be in quadrature with Earth. Additionally, the DKIST will be sensitive enough to measure Zeeman-induced, coronal circular polarization at the limb (*e.g.*, Keil et al. 2011). Coordinated observations between Solar Orbiter and the ground-based CoMP and DKIST will then provide unique datasets to compare 3D magnetic field reconstruction methods and more reliably infer the 3D properties of the coronal magnetic field that trigger solar flares and CMEs.

We thank the anonymous referee and Rebecca Centeno Elliott for a careful consideration of the manuscript and helpful comments. K.D., A.S., S.G., Y.F. and E.D.L. acknowledge support from the Air Force Office of Scientific Research, FA9550-15-1-0030. This work was further supported by the Computational and Information Systems Laboratory, and the High Altitude Observatory. K.D. gratefully acknowledges the support of the french Centre National d'Études Spatiales. The calculations presented in this paper were performed using HPC resources from CALMIP (Grant 2018-2019 [P1504]). The National Center for Atmospheric Research is sponsored by the National Science Foundation.

REFERENCES

- Alissandrakis, C. E. 1981, *A&A*, 100, 197
 Amari, T. & Aly, J.-J. 2010, *A&A*, 522, A52
 Amari, T., Aly, J.-J., Canou, A., & Mikic, Z. 2013, *A&A*, 553, A43
 Amari, T., Boulmezaoud, T. Z., & Aly, J. J. 2006, *A&A*, 446, 691
 Amari, T., Canou, A., Aly, J.-J., Delyon, F., & Alauzet, F. 2018, *Nature*, 554, 211
 Antiochos, S. K., DeVore, C. R., & Klimchuk, J. A. 1999, *ApJ*, 510, 485
 Arnaud, J. & Newkirk, Jr., G. 1987, *A&A*, 178, 263
 Aulanier, G., Janvier, M., & Schmieder, B. 2012, *A&A*, 543, A110
 Barbey, N., Guennou, C., & Auchère, F. 2013, *Sol. Phys.*, 283, 227
 Bateman, G. 1978, *MHD instabilities*
 Bąk-Stęślicka, U., Gibson, S. E., Fan, Y., et al. 2013, *ApJ*, 770, L28
 Bobra, M. G., van Ballegoijen, A. A., & DeLuca, E. E. 2008, *ApJ*, 672, 1209
 Bommier, V. & Sahal-Brechot, S. 1982, *Sol. Phys.*, 78, 157
 Casini, R. & Judge, P. G. 1999, *ApJ*, 522, 524
 Centeno, R., Trujillo Bueno, J., & Asensio Ramos, A. 2010, *ApJ*, 708, 1579
 Charvin, P. 1965, *Annales d'Astrophysique*, 28, 877
 Contopoulos, I., Kalapotharakos, C., & Georgoulis, M. K. 2011, *Sol. Phys.*, 269, 351
 Dalmasse, K., Nychka, D., Gibson, S., Fan, Y., & Flyer, N. 2016, *Frontiers in Astronomy and Space Sciences*, 3, 24
 De Rosa, M. L., Schrijver, C. J., Barnes, G., et al. 2009, *ApJ*, 696, 1780
 DeRosa, M. L., Wheatland, M. S., Leka, K. D., et al. 2015, *ApJ*, 811, 107
 Fan, Y. 2012, *ApJ*, 758, 60
 Feng, X., Jiang, C., Xiang, C., Zhao, X., & Wu, S. T. 2012, *ApJ*, 758, 62
 Forbes, T. G. 2000, *J. Geophys. Res.*, 105, 23153
 Forbes, T. G., Linker, J. A., Chen, J., et al. 2006, *Space Sci. Rev.*, 123, 251
 Frazin, R. A. 2000, *ApJ*, 530, 1026
 Frazin, R. A., Kamalabadi, F., & Weber, M. A. 2005, *ApJ*, 628, 1070
 Freeland, S. L. & Handy, B. N. 1998, *Sol. Phys.*, 182, 497
 Gary, G. A. 2001, *Sol. Phys.*, 203, 71
 Gibson, S. 2015, in *Astrophysics and Space Science Library*, Vol. 415, Solar Prominences, ed. J.-C. Vial & O. Engvold, 323
 Gibson, S., Kucera, T., White, S., et al. 2016, *Frontiers in Astronomy and Space Sciences*, 3, 8
 Gibson, S. E., Dalmasse, K., Rachmeler, L. A., et al. 2017, *ApJ*, 840, L13
 Gorbachev, V. S. & Somov, B. V. 1989, *Soviet Ast.*, 33, 57
 Grad, H. & Rubin, H. 1958, in *Proc. of the Second UN International Atomic Energy Conf. 31, Peaceful Uses of Atomic Energy*
 Guennou, C., Auchère, F., Soubrié, E., et al. 2012, *ApJS*, 203, 25
 Hanle, W. 1924, *Zeitschrift für Physik*, 30, 93
 Harvey, J. W. 1969, PhD thesis
 Hood, A. W. & Priest, E. R. 1981, *Geophysical and Astrophysical Fluid Dynamics*, 17, 297
 Huang, Z., Frazin, R. A., Landi, E., et al. 2012, *ApJ*, 755, 86
 Iman, R. L., Helton, J. C., & Campbell, J. E. 1981, *Journal of Quality Technology*, 13, 174
 Inoue, S., Kusano, K., Magara, T., Shiota, D., & Yamamoto, T. T. 2011, *ApJ*, 738, 161
 Inoue, S., Magara, T., Watari, S., & Choe, G. S. 2012, *ApJ*, 747, 65
 Jiang, C., Wu, S. T., Yurchyshyn, V., et al. 2016, *ApJ*, 828, 62
 Judge, P. G. 1998, *ApJ*, 500, 1009
 Judge, P. G. 2007, *ApJ*, 662, 677
 Judge, P. G., Low, B. C., & Casini, R. 2006, *ApJ*, 651, 1229
 Karna, N., Savcheva, A., Dalmasse, K., et al. submitted, *ApJ*
 Keil, S. L., Rimmele, T. R., Wagner, J., Elmore, D., & ATST Team. 2011, in *Astronomical Society of the Pacific Conference Series*, Vol. 437, Solar Polarization 6, ed. J. R. Kuhn, D. M. Harrington, H. Lin, S. V. Berdyugina, J. Trujillo-Bueno, S. L. Keil, & T. Rimmele, 319
 Kramar, M., Inhester, B., Lin, H., & Davila, J. 2013, *ApJ*, 775, 25

- Kramar, M., Jones, S., Davila, J., Inhester, B., & Mierla, M. 2009, *Sol. Phys.*, 259, 109
- Kramar, M., Lin, H., & Tomczyk, S. 2016, *ApJ*, 819, L36
- Kuhn, J. R., Penn, M. J., & Mann, I. 1996, *ApJ*, 456, L67
- Kusano, K., Bamba, Y., Yamamoto, T. T., et al. 2012, *ApJ*, 760, 31
- Lagg, A., Lites, B., Harvey, J., Gosain, S., & Centeno, R. 2017, *Space Sci. Rev.*, 210, 37
- Lin, H., Kuhn, J. R., & Coulter, R. 2004, *ApJ*, 613, L177
- Lin, H., Penn, M. J., & Tomczyk, S. 2000, *ApJ*, 541, L83
- Low, B. C. 1996, *Sol. Phys.*, 167, 217
- Malanushenko, A., Schrijver, C. J., DeRosa, M. L., Wheatland, M. S., & Gilchrist, S. A. 2012, *ApJ*, 756, 153
- McKay, M. D., Beckman, R. J., & Conover, W. J. 1979, *Technometrics*, 21, 239
- Mikić, Z., Linker, J. A., Schnack, D. D., Lionello, R., & Tarditi, A. 1999, *Physics of Plasmas*, 6, 2217
- Morton, R. J., Tomczyk, S., & Pinto, R. F. 2016, *ApJ*, 828, 89
- Pariat, E., Leake, J. E., Valori, G., et al. 2017, *A&A*, 601, A125
- Penn, M. J. 2014, *Living Reviews in Solar Physics*, 11, 2
- Plowman, J. 2014, *ApJ*, 792, 23
- Priest, E. R. 2003, *Solar magnetohydrodynamics*, ed. B. N. Dwivedi & F. b. E. N. Parker, 217–237
- Querfeld, C. W. 1982, *ApJ*, 255, 764
- Rachmeler, L. A., Gibson, S. E., Dove, J. B., DeVore, C. R., & Fan, Y. 2013, *Sol. Phys.*, 288, 617
- Rachmeler, L. A., Platten, S. J., Bethge, C., Seaton, D. B., & Yeates, A. R. 2014, *ApJ*, 787, L3
- Raouafi, N. E., Riley, P., Gibson, S., Fineschi, S., & Solanki, S. K. 2016, *Frontiers in Astronomy and Space Sciences*, 3, 20
- Sahal-Brechot, S., Bommier, V., & Leroy, J. L. 1977, *A&A*, 59, 223
- Savcheva, A., Pariat, E., McKillop, S., et al. 2016, *ApJ*, 817, 43
- Savcheva, A. S., van Ballegoijen, A. A., & DeLuca, E. E. 2012, *ApJ*, 744, 78
- Schrijver, C. J., De Rosa, M. L., Title, A. M., & Metcalf, T. R. 2005, *ApJ*, 628, 501
- Shibata, K. & Magara, T. 2011, *Living Reviews in Solar Physics*, 8, 6
- Somov, B. V. & Verneta, A. I. 1993, *Space Sci. Rev.*, 65, 253
- Su, Y., Surges, V., van Ballegoijen, A., DeLuca, E., & Golub, L. 2011, *ApJ*, 734, 53
- Titov, V. S., Downs, C., Mikić, Z., et al. 2018, *ApJ*, 852, L21
- Titov, V. S., Török, T., Mikic, Z., & Linker, J. A. 2014, *ApJ*, 790, 163
- Tomczyk, S., Card, G. L., Darnell, T., et al. 2008, *Sol. Phys.*, 247, 411
- Tomczyk, S., Landi, E., Burkepile, J. T., et al. 2016, *Journal of Geophysical Research (Space Physics)*, 121, 7470
- Tziotziou, K., Georgoulis, M. K., & Raouafi, N.-E. 2012, *ApJ*, 759, L4
- Valori, G., Kliem, B., & Keppens, R. 2005, *A&A*, 433, 335
- Valori, G., Kliem, B., Török, T., & Titov, V. S. 2010, *A&A*, 519, A44
- van Ballegoijen, A. A. 2004, *ApJ*, 612, 519
- van Ballegoijen, A. A., Priest, E. R., & Mackay, D. H. 2000, *ApJ*, 539, 983
- Van Vleck, J. H. 1925, *Proceedings of the National Academy of Science*, 11, 612
- Wheatland, M. S. 2007, *Sol. Phys.*, 245, 251
- Wheatland, M. S., Sturrock, P. A., & Roumeliotis, G. 2000, *ApJ*, 540, 1150
- Wiegelmann, T. 2004, *Sol. Phys.*, 219, 87
- Wiegelmann, T. & Inhester, B. 2010, *A&A*, 516, A107
- Wiegelmann, T. & Sakurai, T. 2012, *Living Reviews in Solar Physics*, 9, 5
- Wiegelmann, T., Thalmann, J. K., Inhester, B., et al. 2012, *Sol. Phys.*, 281, 37
- Wiegelmann, T., Thalmann, J. K., & Solanki, S. K. 2014, *A&A Rev.*, 22, 78
- Yang, W. H., Sturrock, P. A., & Antiochos, S. K. 1986, *ApJ*, 309, 383
- Yeates, A. R. 2014, *Sol. Phys.*, 289, 631
- Yeates, A. R., Amari, T., Contopoulos, I., et al. 2018, *Space Sci. Rev.*, 214, 99
- Yeates, A. R., Mackay, D. H., & van Ballegoijen, A. A. 2007, *Sol. Phys.*, 245, 87
- Zhu, X. S., Wang, H. N., Du, Z. L., & Fan, Y. L. 2013, *ApJ*, 768, 119
- Zuccarello, F. P., Pariat, E., Valori, G., & Linan, L. 2018, *ApJ*, 863, 41